Biophysical Journal
Article

Addressing spatiotemporal signal variations in pair correlation function analysis

Vahid Khandan,[1] Vincent J. P. Boerkamp,[2] Ryan C. Chiechi,[3] Johannes Hohlbein,[2,4,*] and Klaus Mathwig[1,5,*]
[1]University of Groningen, Groningen Research Institute of Pharmacy, Pharmaceutical Analysis, Groningen, the Netherlands; [2]Laboratory of Biophysics, Wageningen University & Research, Wageningen, the Netherlands; [3]Department of Chemistry & Organic and Carbon Electronics Laboratory, North Carolina State University, Raleigh, North Carolina; [4]Microspectroscopy Research Facility, Wageningen University & Research, Wageningen, the Netherlands; and [5]imec within OnePlanet Research Center, Wageningen, the Netherlands

ABSTRACT Fluorescence correlation spectroscopy (FCS) is a cornerstone technique in optical microscopy to measure, for example, the concentration and diffusivity of fluorescent emitters and biomolecules in solution. The application of FCS to complex biological systems, however, is fraught with inherent intricacies that impair the interpretation of correlation patterns. Critical among these intricacies are temporal variations beyond diffusion in the quantity, intensity, and spatial distribution of fluorescent emitters. These variations introduce distortions into correlated intensity data, thus compromising the accuracy and reproducibility of the analysis. This issue is accentuated in imaging-based approaches such as pair correlation function (pCF) analysis due to their broader regions of interest compared with point-detector-based approaches. Despite ongoing developments in FCS, attention to systems characterized by a spatiotemporal-dependent probability distribution function (ST-PDF) has been lacking. To address this knowledge gap, we developed a new analytical framework for ST-PDF systems that introduces a dual-timescale model function within the conventional pCF analysis. Our approach selectively differentiates the signals associated with rapid processes, such as particle diffusion, from signals stemming from spatiotemporal variations in the distribution of fluorescent emitters occurring at extended delay timescales. To corroborate our approach, we conducted proof-of-concept experiments on an ST-PDF system, wherein the, initially, uniform distribution of fluorescent microspheres within a microfluidic channel changes into a localized accumulation of microspheres over time. Our framework is offering a comprehensive solution for investigating various phenomena such as biomolecular binding, sedimentation, and particle accumulation.

SIGNIFICANCE Fluorescence correlation spectroscopy (FCS) is an important technique to extract a variety of quantitative molecular information in microscopy. State-of-the-art FCS data analysis, i.e., the correlation analysis of a series of images of fluorescent emitters such as nanoparticles or dye molecules, struggles with analyzing complex overlapping patterns such as movement of emitters occurring at different timescales. Here, we overcome this limitation by introducing a new technique of analyzing FCS images. We demonstrate its broad applicability by distinguishing drift and diffusion of fluorescent nanoparticle in a microfluidic setup. Our method is of significance for a variety of phenomena studied using FCS such as molecular binding, aggregation of transport of fluorescent emitters.

INTRODUCTION

Fluorescence correlation spectroscopy (FCS) is a pivotal technique that quantifies the properties of systems by correlating the fluctuations in emitted light intensity with the dynamics of suspended fluorescent entities (emitters). Despite its significant benefits, the application of FCS to complex environments such as living cells is impeded by challenges including cellular heterogeneity, biomolecular crowding, confinement of the medium, and accelerated photobleaching (1). These obstacles have spurred an increasing demand for advancements in conventional FCS (2–4). The advent of advanced FCS techniques such as single plane illumination microscopy FCS (5,6), two-photon FCS (7), inverse FCS (8), stimulated emission depletion FCS (9), dual-color fluorescence cross-correlation spectroscopy (10), multifocus FCS (11), parallel and perpendicular scanning FCS (12), space-time image correlation spectroscopy (13), and pair correlation function (pCF) (14) stems from this standpoint (4).

Submitted April 17, 2024, and accepted for publication August 2, 2024.

*Correspondence: johannes.hohlbein@wur.nl or klaus.mathwig@imec.nl

Vahid Khandan and Vincent J.P. Boerkamp contributed equally to this work.

Editor: Elizabeth Rhoades.

https://doi.org/10.1016/j.bpj.2024.08.002

Progress in FCS has been driven not only by innovations in instrumentation but also by novel approaches in data processing. These approaches were developed as the accuracy of FCS-based analysis depends on the validity of the model function employed to describe the system (2,4). A valid model function must characterize all processes governing the dynamics of the system as the sources of fluctuations in the intensity of the detected light. However, the correlation patterns reflect the collective properties of all sources, rather than specifically the phenomenon under investigation (3,15). Consequently, the model function must distinguish the data set of interest (e.g., particle diffusion) from the data associated with extraneous sources of fluctuations (4,15).

In steady-state systems, intensity fluctuations arise from variations in both the intensity of individual emitters and their spatial distribution. Assuming a constant intensity for individual emitters and a constant probability density function (PDF) for their spatial distribution, the average of instantaneous changes in the number of emitters becomes negligible over extended delay times. Under these conditions, correlated intensities are accurately characterized by well-established model functions describing the diffusion and transport of fluorescent emitters (1,3). However, processes involving a spatiotemporal-dependent PDF (ST-PDF) yield variations in both the number and spatial distribution of emitters, resulting in substantial distortions in the shape of spatially correlated intensities. This complicates the interpretation of FCS data using conventional model functions, adversely affecting the accuracy and reproducibility of the processed data and potentially rendering the FCS technique ineffective (3,16). Examples of such processes include particle aggregation, biomolecule-associated vesicle formation, biomolecule immobilization, photobleaching-induced emitter depletion, and nonequilibrium conditions resulting in local accumulation of emitters (16–24).

So far, several model functions have been introduced to account for data distortions by adding components to conventional model functions (3,25,26). However, the abstract nature of correlated data and the complexity of the system make it challenging to characterize fluctuations using separate components. Even a comprehensive model function that accounts for all sources of fluctuations can struggle to extract useful information due to limited fitting parameters. Overspecifying the model with excessive degrees of freedom may lead to overfitting of data, which obscures the underlying pattern and complicates the fitting of multicomponent model functions. Moreover, existing model functions are only effective for specific, limited sources of distortion, such as photobleaching (27) or biomolecular binding (28), with little attention given to processes like particle accumulation involving long-persistent changes in emitter quantities over time. Alternative techniques include collecting multiple short stacks instead of a single extended stack (29), discarding distorted frames (3,16), or removing artifacts using AI-based pipelines (30). Nonetheless, these methods are time-consuming and ineffective when the source of distortion persists over long delay times. These limitations necessitate isolating the experimental setup from extraneous sources of fluctuations, such as ensuring proper sample preparation and preventing fluorophore aggregation (31). However, these precautions alone may not be sufficient.

In addressing the scientific gap, our study introduces a new dual-timescale model function tailored for ST-PDF systems. Our approach separates fast processes such as diffusion from slower processes such as temporal variations in the spatial distribution of emitters. To accomplish this, we have employed the pCF technique as the basis platform to nest our dual-timescale model function. The pCF technique is particularly beneficial for handling anisotropy and inhomogeneity common in ST-PDF systems (14,32–34). Using a microfluidic setup that we developed previously (35), we created nonequilibrium conditions to change an initially uniform distribution of nanospheres into a localized particle group, forming an ST-PDF system for analysis. We show the limitations of traditional pCF in dissecting these systems arising due to due to convoluted correlated data. We then demonstrate how our approach can deconvolve processes based on their different characteristic timescales.

Our dual-timescale model function offers a new way of performing diffusometry and velocimetry in anisotropic and inhomogeneous ST-PDF systems under nonequilibrium conditions. It promises exploration of a range of phenomena exhibiting temporal change of spatial emitter distributions such as sedimentation (36), biomolecular binding (28), particle accumulation (37), and multiple phoretic motions (38,39).

MATERIALS AND METHODS

Materials

Carboxylated polystyrene microspheres (FluoSpheres) with a nominal diameter of 0.02 μm and excitation/emission wavelengths of 505/515 nm were obtained from Thermo Fisher Scientific (Eugene, OR), catalog number F8811, and were stored at 4°C. The chemicals needed for surface treatment of microfluidic channels, including succinic anhydride (SA), (3-aminopropyl)triethoxysilane (APTES), absolute ethanol, and dimethylformamide (DMF), were purchased from Sigma-Aldrich (Amsterdam, the Netherlands). For soft lithography and photolithography processes, poly(dimethylsiloxane) (PDMS) from Dow Corning (Midland, MI) (SYLGARD 184) and SU8 negative photoresists (SU8-2002 and SU8-2100) from MicroChem (Newton, MA) were used, respectively. Surface activation was performed using a Harrick Plasma (Ithaca, NY) machine. Flow within the microfluidic device was facilitated using Harvard Apparatus syringe pumps, glass micro-syringes from ILS (Ilmenau, Germany), and Tygon tubing with inner and outer diameters of 0.25/0.76 mm, obtained from Avantor VWR (Radnor, PA).

Device fabrication and surface treatment

Microfluidic devices (see Fig. 1 *a*) were fabricated using a replica molding process. Initially, the master mold, containing the reverse shape of the designed microfluidic structures, was fabricated using clean room

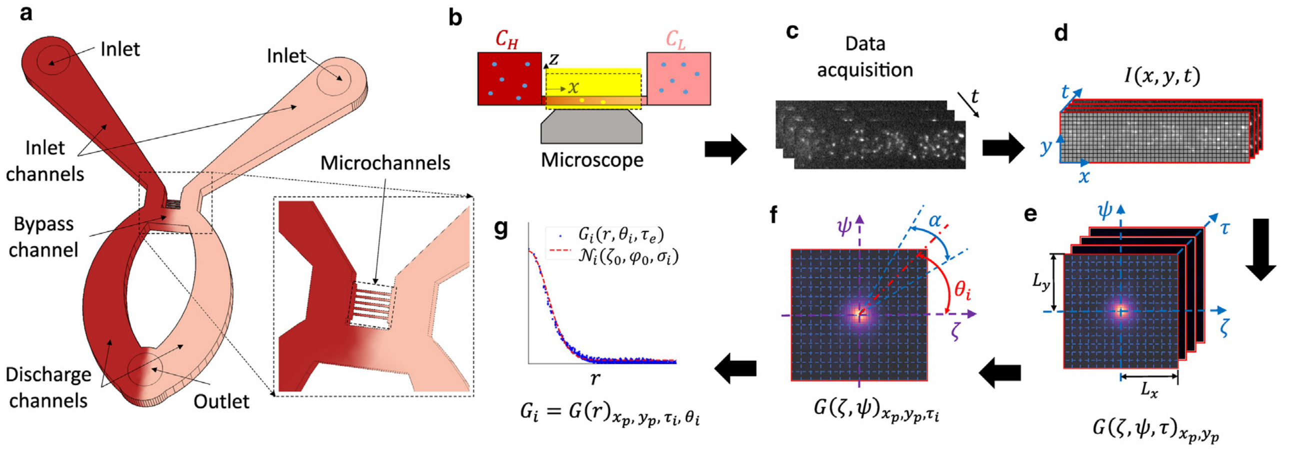

FIGURE 1 Overview of the experimental setup and data processing using pCF. (*a*) Isometric view of the microfluidic gradient generator and (*b*) side view of the established glycerol concentration gradient within the mixing microchannel. (*c*) Capturing the instantaneous spatial distribution of the fluorescent nanospheres using fluorescence microscopy and (*d*) converting image stacks into the intensity signal function, $I(x,y,t)$. (*e*) Calculation of the pair correlation function, $G(\zeta,\psi,\tau)$, from the spatiotemporal correlation of the signal function at a point (x_p,y_p) relative to its neighboring pixels $(x_p+\zeta,y_p+\psi)$ situated within the relative padding distances L_x and L_y, over a delay time τ. (*f*) Discretization of $G(\zeta,\psi,\tau)$ into N angular sectors $(\theta_{i=1,2,3,\ldots,N})$ with a constant span of $\alpha = \frac{2\pi}{N}+\alpha_p$ for each delay time τ_e. The term α_p is the constant angular overlap between any two adjacent sectors. (*g*) Fitting N one-dimensional Gaussian distributions, $\mathcal{N}_i(\zeta_0,\psi_0,\sigma_i)$, to evaluate temporal variations in the position of the Gaussian mean $(\zeta_0(\tau_e),\psi_0(\tau_e))$ and directional variance $\sigma_i(\tau_e)$, to quantify local velocity vector and the diffusivity tensor.

photolithography. The surface was patterned in two steps to create two layers of different thicknesses. The first layer, containing shallow microchannels with a height of 2 μm, was made using SU-8 2002 negative photoresist, while the rest of the design layout, such as side channels, was shaped in the second layer with a thickness of 200 μm using SU-8 2100 negative photoresist. The chromium photomask for both layers was obtained from DeltaMask (Twente, the Netherlands), and prebaking, exposure, postbaking, and hard baking was conducted according to the guidelines provided by the photoresist data sheet from MicroChem, except for postbaking of SU-8 2100, which was done at 65°C for 15 min in one step.

Subsequently, the patterned structures were transferred from the master mold to PDMS using the soft lithography technique, performed outside the cleanroom environment. A prepolymer solution of PDMS and a curing agent at a 10:1 (w/w) ratio was poured onto the mold and cured on a leveled hotplate at 70°C for 2 h. Afterward, the elastic layer was peeled off, the devices were separated by cutting, and the inlet and outlet holes were created using a 1 mm biopsy punch. Finally, the PDMS layer and a glass coverslip were cleaned using an air gun and scotch tape and activated with oxygen plasma for 25 s at a pressure of 310–320 mTorr. The activated PDMS and glass were immediately bonded without applying pressure and placed on a hotplate at 70°C for 2 min to strengthen the bonding.

A stepwise surface modification process was adopted to introduce carboxyl groups (-COOH) onto the interior surface of the microfluidic device. Matching the functional groups of carboxylate microsphere, adsorption of sphere is, thus, prevented effectively. In the first step, a 5% (v/v%) solution of APTES in absolute ethanol was introduced immediately after PDMS-glass bonding to interact with hydroxyl linkers (-OH) generated during plasma activation, leaving amine groups (-NH_2) on the surface. After 30 min, the silane solution was flushed out, followed by rinsing with absolute ethanol and then DMF. A solution of 25 mM SA in DMF was then introduced to react with the NH_2 groups to create carboxyl groups. Microfluidic devices were placed on a hotplate at 100°C for 2 h, and the SA solution was flushed out with DMF. After completing the surface treatment, Milli-Q water was used to flush out the DMF, and the inlet and outlet connections were sealed with scotch tape to preserve the treated chip for further optical measurements.

Before the optical measurement, sodium hydroxide (NaOH) was added to the suspension of carboxylated nanoparticles to deprotonate the hydrogen atom of the carboxyl groups, creating negatively charged surfaces on both the nanoparticles and the interior surface of the microchannel. This prevents nanosphere aggregation and adsorption due to electrostatic repulsion, enhancing the quality of optical measurements.

Fluorescence microscopy

The fluorescence microscopy was conducted using a home-built setup, OpenFrame (40). The setup consists of a multimode laser unit with 640 nm wavelengths (MatchBox, Integrated Optics, Vilnius, Lithuania) operating at 270 mW. The laser output was coupled into a 150 × 150 μm square silica core fiber to promote mode mixing in the fiber, achieving a uniform spatial distribution and a square beam shape, in contrast to the Gaussian profile typical of a single-mode fiber (M102L05, Thorlabs, Newton, NJ) (41,42). Moreover, an oil immersion objective (Apo TIRF 60× 1.49 NA, Nikon, Tokyo, Japan), a double band emission filter (ZET 532/640m-TRF), and a camera (Prime 95B sCMOS, Photometrics, Tucson, AZ) were implemented to reach an effective pixel size of 180 nm. The setup was controlled by the micromanager 1.4 software package (43,44), whereas the frame time was externally controlled in accordance with the laser pulses using a home-built program, SMILE (45). Before data acquisition, camera images were cropped to the dimensions a single microchannel to enable acquisition speeds of 500 fps.

pCF analysis

pCF analysis is performed using a MATLAB script that loads the collected stack images to obtain the intensity data, $I(x,y,t)$, where x and y denote the position of pixels within the observation area, and t represents the frame time. As depicted in Fig. 1, the pCF, $G(\zeta,\psi,\tau)$, is calculated for all pixels by assessing the spatiotemporal correlation of $I(x,y,t)$ at a given pixel (x_p,y_p) as

$$G(\zeta,\psi,\tau) = \frac{\langle I(x_p,y_p,t).\, I(x_p+\zeta,y_p+\psi,t+\tau)\rangle_t}{\langle I(x_p,y_p,t)\rangle_t \cdot \langle I(x_p+\zeta,y_p+\psi,t)\rangle_t} - 1. \tag{1}$$

Here, $\langle \ldots \rangle_t$ signifies the time average, τ denotes the delay time, and $-L_x \le \zeta \le L_x$, and $L_y \le \psi \le L_y$ are the distances from the reference pixel at (x_p, y_p) in the x and y directions, respectively, within a padding box of dimensions $2L_x$ and $2L_y$ (32,33). In all experiments, the padding distance is $L_x = L_y = 4.545\ \mu\text{m}$, equal to 25 pixels, given a pixel size of 180 nm. The delay time, τ, is set at 2 ms, matching the frame time of the recorded image stacks.

To facilitate data processing, the spatiotemporal correlation between the signal intensity data at (x_p, y_p), $I_a = I(x_p, y_p, t)$, and its shifted counterpart, $I_b = I(x_p + \zeta, y_p + \psi, t + \tau)$, is determined from the convolution of I_a and I_b signals. The mathematical expression for this approach is given as (32,33).

$$(I_a \bigstar I_b)_{(\zeta,\psi,\tau)} = \mathcal{F}^{-1}\left\{\mathcal{F}_a^* \times \mathcal{F}_b\right\} \tag{2}$$

Here, $\mathcal{F}_a^*$ represents the complex conjugate of the Fourier transform of I_a, while $\mathcal{F}_b$ stands for the Fourier transform of I_b. The symbol $\mathcal{F}^{-1}\{\}$ denotes the inverse Fourier transform, and $\bigstar$ denotes convolution.

The convoluted data is then normalized relative to the real values of $\mathcal{F}_a^*$ and $\mathcal{F}_b$ at zero delay to determine $G(\zeta, \psi, \tau)$ as

$$G(\zeta, \psi, \tau) = N \frac{\mathcal{F}^{-1}\left\{\mathcal{F}_a^* \times \mathcal{F}_b\right\}}{\mathcal{R}e\left(\mathcal{F}_a\big|_{\tau=0}\right) \mathcal{R}e\left(\mathcal{F}_b\big|_{\tau=0}\right)} - 1 \tag{3}$$

where N represents the total number of stacks. This calculation is performed using the fast Fourier transform algorithm on a GPU, taking circular cross-correlation into account.

The calculated $G(\zeta, \psi, \tau)$ is then segmented into eight angular sectors for every delay time, τ_e, up to 40 ms. As illustrated in Fig. 1 *f*, these sectors are identified by $\left|\theta - \theta_{i=1,2,3,..,8}\right| \le \frac{\alpha}{2}$, where (r, θ) are the polar coordinates corresponding to the distances $(\zeta - \zeta_0(\tau_e), \psi - \psi_0(\tau_e))$. Here, $\theta_i = \frac{2\pi i}{8}$ is the central angle of each sector, and $\alpha = \frac{2\pi}{8} + \alpha_p$ is the angular width of each sector. The term $\alpha_p = \frac{\pi}{8}$ ensures a constant angular overlap between adjacent sectors.

Subsequently, eight one-dimensional Gaussian distributions, each sharing the same mean value as specified in Eq. 7, are fitted across the segmented pCF, $G(r, \theta_i)$, for all sectors to ascertain the Gaussian mean position $(\zeta_0(\tau_e), \psi_0(\tau_e))$ and the directional mean-squared displacement, $\text{MSD}(\theta_\text{i}, \tau_\text{e})$, for each delay time τ_e. To improve fitting accuracy for pixel points near the center, a weighting function mirroring the distribution of the segmented pCF is applied. Fittings with a normalized root mean-square error over 0.1 are discarded to ensure data reliability. Finally, the linear models $\zeta_0(\tau_e) = v_x \tau_e$, $\psi_0(\tau_e) = v_y \tau_e$, and $\text{MSD}(\theta_i, \tau_e) = 4D(\theta_i)\tau_e$ were applied to the quantified values of $(\zeta_0(\tau_e), \psi_0(\tau_e))$ and $\text{MSD}(\theta_i, \tau_e)$ for τ_e up to 30 and 20 ms, respectively, to determine the components of the local velocity vector (v_x, v_y) and the diffusivity tensor D_θ.

RESULTS AND DISCUSSION

We used a microfluidic device to create a time-dependent inhomogeneous distribution of suspended fluorescent nanospheres thereby representing an ST-PDF distribution. The microfluidic device illustrated in Fig. 1 generates a stable glycerol concentration gradient along a microchannel connecting two side channels with aqueous solutions of different glycerol concentrations. This concentration gradient changes the viscosity of the solution, creating an inhomogeneous medium in which the diffusivity of suspended nanospheres varies (46). Within this inhomogeneous medium, a range of transport phenomena including Poiseuille flow, diffusiophoresis, diffusioosmosis, and viscophoresis can arise, each exerting an independent driving impact on the suspended nanospheres in various directions (see supporting material) (39,47–52).

We have previously demonstrated that the interplay of these transport mechanisms transforms the initially uniform distribution of fluorescent nanospheres into a localized accumulation within the microchannel, aligning with an ST-PDF model (35). To capture the instantaneous spatial distribution of nanospheres, we combined the microfluidic device with a custom-built fluorescence microscope. The microscope is equipped with uniform flat-field illumination (42), facilitating observation across the entire microchannel. We then processed recorded image stacks to extract the fluctuations in pixel intensities, essential for calculating local pCFs.

pCF analysis of ST-PDF systems

The calculated pCF for each pixel point at a given position, $G(\zeta, \psi, \tau)$, provides insight into the instrument's performance and the dynamics of the diffusing nanospheres, expressed as

$$G(\zeta, \psi, \tau) = P(\zeta, \psi, \tau) \otimes W(\zeta, \psi) \tag{4}$$

Here, $P(\zeta, \psi, \tau)$ is the PDF characterizing the dynamics of the nanospheres, $\otimes$ denotes the convolution operator, and $W(\zeta, \psi)$ represents the instrument's point spread function (32,33).

$P(\zeta, \psi, \tau)$ determines the probability of an emitter, initially located at the reference position (x_p, y_p), being found at a neighboring pixel position $(x_p + \zeta, y_p + \psi)$ after a delay time of τ. In systems with a consistent quantity of emitters and minimal spatial variations in their number density, fluctuations in intensity are exclusively attributed to the diffusion and transport of the emitters. Under these conditions, $P(\zeta, \psi, \tau)$ follows a Gaussian distribution, where changes in its mean value and variance—its first and second moments—reflect the emitters' drift velocity and diffusion, respectively (14,33,53). However, this standard model function becomes invalid in ST-PDF systems because emitters are more likely found in areas with a higher number density. In such systems, the temporal changes in the spatial distribution of emitters add another source of intensity fluctuations, which must be considered in the interpretation of $G(\zeta, \psi, \tau)$ (4).

Fig. 2 illustrates the impact of experimental spatiotemporal variations in the distribution of nanospheres on the pCF analysis. The data show that, initially, uniformly distributed nanospheres (Fig. 2 *a*) form a localized accumulation in the microchannel due to the glycerol concentration gradient (Fig. 2 *b*). As expected, for pixel points far from the accumulation zone, $G(\zeta, \psi, \tau)$ aligns with the standard Gaussian model, which shows that diffusion and transport are the only processes at play. Conversely, the pCFs corresponding to pixels near the accumulation zone exhibit significant distortion, making the standard Gaussian model function inapplicable. Notably, this distortion in the calculated $G(\zeta, \psi, \tau)$ closely matches the nanosphere

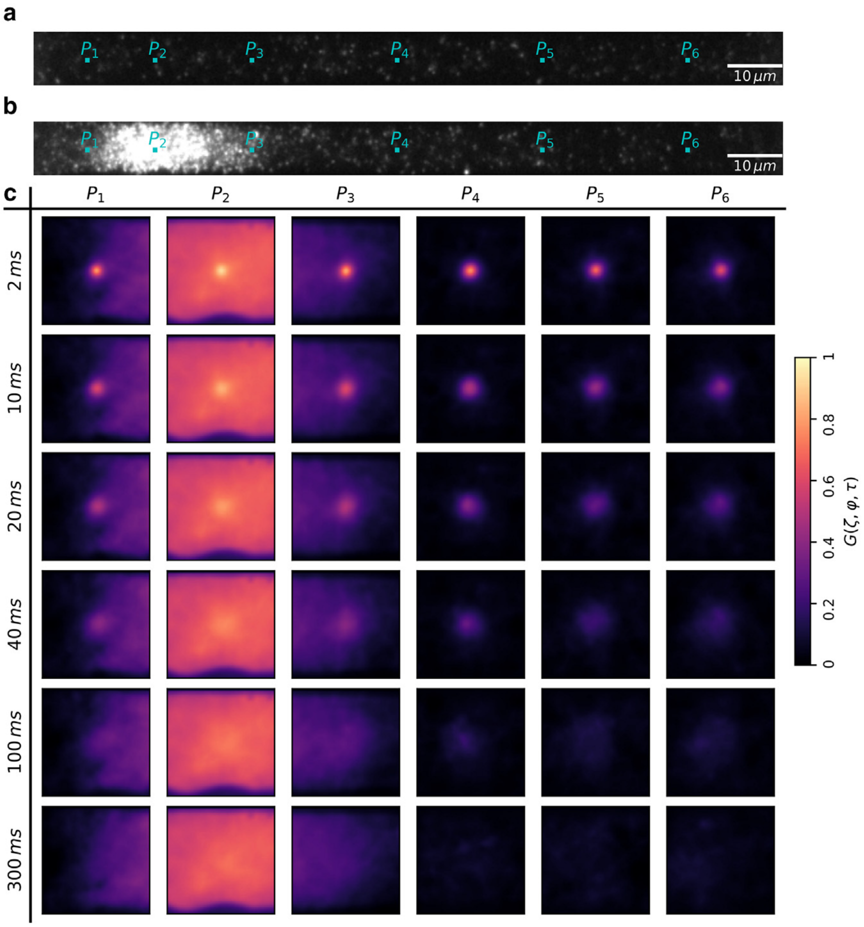

FIGURE 2 Distorted pCF in an ST-PDF system. The initially uniform distribution of fluorescent nanospheres (*a*) transforms into localized accumulation (*b*) in response to the constant aqueous glycerol gradients of 50 and 10% (w/w%) applied at the left and right ends of the mixing microchannel, respectively. (*c*) The temporal variations in $G(\zeta, \psi, \tau)$, calculated for six pixels, P_1 to P_6, with positions specified in (*a*) and (*b*). The Gaussian pattern within $G(\zeta, \psi, \tau)$, reflecting the diffusion and transport of the nanospheres, quickly dissipate within 300 ms, while the convolution arising from particle accumulation persists. The values of $G(\zeta, \psi, \tau)$ for each pixel point are normalized against their respective peak values at $\tau = 2$ ms.

accumulation pattern, suggesting increased $P(\zeta, \psi, \tau)$ values in areas with a higher number density of nanospheres.

Nevertheless, the variations in $G(\zeta, \psi, \tau)$ over different delay times τ, shown in Fig. 2 *c*, indicate that intensity from nanosphere transport and diffusion quickly decreases, while data from particle accumulation remains constant over short delay times. Importantly, a delay time of $\tau = 300$ ms is adequate for the relaxation of the signals from the fast-paced processes of transport and diffusion, but not enough for the slower-paced accumulation of nanospheres to change $G(\zeta, \psi, \tau)$. Therefore, although $G(\zeta, \psi, \tau)$ reflects the cumulative impact of all processes governing the system's dynamics, its changes over time reveal the differences in these processes, particularly the timescales at which they unfold. This observation inspired the development of the dual-timescale model function introduced in this study.

pCF analysis using a dual-timescale model function

The attenuation of signals from transport and diffusion occurs much faster than signals from temporal variations in the spatial distribution of emitters. Thus, $G(\zeta, \psi, \tau)$ can be expressed as a combination of two separate fast $F(\zeta, \psi, \tau)$, and slow $S(\zeta, \psi, \tau)$ components, such that $G(\zeta, \psi, \tau) = F(\zeta, \psi, \tau) + S(\zeta, \psi, \tau)$. Since the signal attenuation of these two components occurs at distinct timescales, a range of time delays can be identified where the fast component has already dissipated, while the slow component remains unchanged. This time delay will henceforth be referred to as the "signal separation delay time," or τ_s.

Given that at the delay time of τ_s, the fast component has dissipated, the pCF is only the slow component, denoted as $G(\zeta, \psi, \tau_s) = S(\zeta, \psi, \tau_s)$. Furthermore, the slow component remains constant for delay times $\tau \leq \tau_s$, indicating that $S(\zeta, \psi, \tau)$ equals $S(\zeta, \psi, \tau_s)$ within this time period. Consequently, the fast component, $F(\zeta, \psi, \tau)$, can be directly derived from $G(\zeta, \psi, \tau)$ for delay times $\tau \leq \tau_s$ as

$$F(\zeta, \psi, \tau) = G(\zeta, \psi, \tau) - G(\zeta, \psi, \tau_s). \tag{5}$$

The fast component $F(\zeta, \psi, \tau)$, as defined in Eq. 5, is only due to diffusion and transport of emitters and can be described by the standard Gaussian model. In fact, the expression $G(\zeta, \psi, \tau_s) = S(\zeta, \psi, \tau_s)$ selectively segregates the convoluted data within the overall correlated data set,

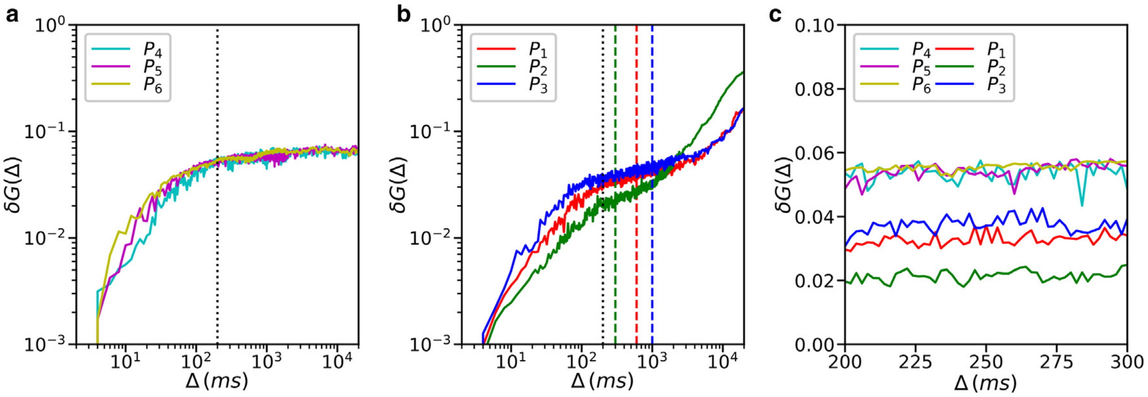

FIGURE 3 Quantitative analysis of the operational timescales of fast and slow components of pCF. $\delta G(\Delta)$ values are calculated using Eq. 6 for pixel points P_1 to P_6 as indicated in Fig. 2. An immediate increase in $\delta G(\Delta)$ is noted for both groups of pixel points: those within (*b*) and those distant (*a*) from the accumulation zone. This initial phase concludes around $\tau_{FT} = 200$ ms (indicated by *black dotted line*), signaling the dissipation of the fast component *F*. The start of the final phase, τ_{ST} (represented by *dashed lines* in the same color as the corresponding data points), showcasing the impact of the slow component (*S*), is not observed in pixels outside the accumulation zone (*a*). In contrast, it is distinctly noticeable at varying delay times for pixels within the zone. Although the identified values for τ_{ST} depends on the location of the pixel points relative to the accumulation zone, a range of 200 ms $\leq \tau_s \leq$ 300 ms is considered as the signal separation time delay, since the respective $\delta G(\Delta)$ values align within the plateau of the intermediate phase (*c*). The formation of the nanosphere accumulation zone is attributed to the constant aqueous glycerol gradients of 50 and 10% (w/w%) applied at the left and right ends of the mixing microchannel, respectively.

facilitating the interpretation of $G(\zeta,\psi,\tau)$ without requiring extra terms to account for the convolutions.

The signal separation delay time, τ_s, specified in Eq. 5, is the time shift needed for the correlated signals from the rapid processes of transport and diffusion to fully dissipate. Therefore, τ_s represents the delay time at which an emitter has an equal probability of being located anywhere within the cross-correlation box. Consequently, the value of τ_s depends on both the size of the cross-correlation box and the diffusivity of the emitter. However, as the diffusivity of the emitter remains undetermined, an alternate approach is essential to determine this parameter.

A viable strategy for this purpose is screening the attenuation of $G(\zeta,\psi,\tau)$ over both short and extended delay times to identify the range within which the fast (*F*) component has fully dissipated, while the slow (*S*) component remains constant. To accomplish this, we calculated the normalized root mean-squared deviation between pCF at an initial delay time of $\tau = 2$ ms (corresponding to the temporal resolution of our experimental setup), $G_0(\zeta,\psi)$, and at an extended delay time of $\tau = \Delta > 2$ ms. This is defined as

$$\delta G(\Delta) = \sqrt{\frac{\sum \left(G_0(\zeta,\psi) - G(\zeta,\psi,\Delta)\right)^2}{G_{max}\,A_p}}. \tag{6}$$

Here, A_p denotes the area of the cross-correlation box, measured in number of pixels, while G_{max} signifies the peak value of $G_0(\zeta,\psi)$.

Given the distinct timescales at which the *F* and slow *S* components of the pCF operate, the variations in $\delta G(\Delta)$ appear in three sequential phases, each highlighting distinct processes associated with the *F* and *S* components. The initial phase, Λ_1, is characterized by a pronounced increase within short delay times, indicative of the rapid attenuation of the *F* component. This phase concludes once $\delta G(\Delta)$ reaches a nearly constant value, signaling the full dissipation of *F*. Following this, a transient phase Λ_2 emerges, marked by a plateau in $\delta G(\Delta)$, where the *F* component has already dissipated, yet the elapsed delay time remains too brief to reveal any variations driven by the *S* component. The progression to the final phase, Λ_3, is characterized by discernible changes in $\delta G(\Delta)$, signifying the start of variations driven by the *S* component over long delay times. Within this framework, a τ_s value is considered valid if it falls within the interval defined by the end of the first phase, τ_{FT} (marking the complete dissipation of the *F* component), and the start of the third phase, τ_{ST} (indicating no change in the *S* component).

Fig. 3 illustrates the variations in $\delta G(\Delta)$ for two sets of pixel points: those within and those far from the accumulation zone. An immediate increase in $\delta G(\Delta)$ at short delay times signifies the start of the phase Λ_1 associated with the rapid attenuation of the fast (*F*) component. For all considered pixel points, this phase concludes approximately at $\tau_{FT} = 200$ ms, marked by a black dotted line. At this point, $\delta G(\Delta)$ values stabilize at nearly constant levels, signaling the onset of the transition phase Λ_2. Fig. 3 *a* shows that for pixel points outside the accumulation zone, the final phase does not start. Here, the pCF is accurately represented by the *F* component alone, reflecting nanosphere transport and diffusion. Conversely, for the second group of pixel points, the beginning of the final phase is discernible, illustrated by dashed lines in Fig. 3 *b*. Significantly, at the beginning of the phase Λ_3, τ_{ST}, driven by the *S* component, differs among the pixel points within this group. For pixel P_2, located squarely within the accumulation zone, τ_{ST} is notably smaller than those of pixels P_1 and P_3, which are only partially placed within the accumulation zone. This finding suggests that a stronger S component precipitates an earlier initiation of phase Λ_3. Despite these variations in the identified τ_{ST}, a range of 200 ms $\leq \tau_s \leq$ 300 ms satisfies the requirements for a valid signal separation delay time (see Fig. 3 *c*). This interval marks the end of the phase Λ_1 by dissipation of the F component and exhibits minimal signs of the onset of the phase Λ_3, ensuring the stability of the S component.

Fig. 4 *a* shows that when setting τ_s at 200 ms, the pCF, $G(\zeta, \psi, \tau)$, effectively decomposes into its $F(\zeta, \psi, \tau)$ and $S(\zeta, \psi, \tau)$ components for short delay times $\tau \leq \tau_s$. Notably, the slow component $S(\zeta, \psi, \tau)$ selectively subtracts the distortions in $G(\zeta, \psi, \tau)$ attributed to nanosphere accumulation under ST-PDF conditions. Furthermore, it maintains the integrity of the $G(\zeta, \psi, \tau)$ signal for pixel points P_4 to P_6 located away from the accumulation zone. This observation implies that the distortion-free component $F(\zeta, \psi, \tau)$ contains the entirety of the data set related to the transport and diffusion of nanospheres. Thus, the extracted $F(\zeta, \psi, \tau)$ component, representing the transport and diffusion processes, can be adequately described by the standard model functions and serve as a substitute for $G(\zeta, \psi, \tau)$ in pCF analysis. This pattern is evident in Fig. 4 *b*, where the temporal variations of the extracted $F(\zeta, \psi, \tau)$ are displayed over $\tau \leq \tau_s$.

The analysis of pCF data using the standard Gaussian model functions facilitates identifying the position of Gaussian mean and directional variances, which are essential for quantifying drift velocity vectors and diffusivity tensors. This process typically unfolds in two steps of fitting. Initially, the subpixel location of the Gaussian mean is determined using fitting a two-dimensional Gaussian distribution. Subsequently, the pCF is divided into multiple angular sectors based on the determined mean. Directional variance is subsequently ascertained using the fit from a one-dimensional Gaussian distribution over the segmented pCF data. Nevertheless, the interdependence of fitting parameters across both steps suggests that a more precise assessment could be realized through their simultaneous evaluation.

To achieve a more accurate fitting, we propose a model comprising N one-dimensional Gaussian distributions. Each distribution, $\mathcal{N}_i(\zeta_0, \psi_0, \sigma_i)$, evaluates directional variances across N different directions, centered around a common Gaussian mean $\mu = (\zeta_0, \psi_0)$. This model is expressed as

$$\begin{aligned} \mathcal{N}_i(\zeta_0, \psi_0, \sigma_i) &= g_i(\tau) exp \\ &\times \left(- \frac{(\zeta - \zeta_0(\tau))^2 + (\psi - \psi_0(\tau))^2}{\sigma_i(\tau)^2} \right), \\ i &= 1, 2, 3, .., N. \end{aligned} \tag{7}$$

Here, $g_i(\tau) = \frac{\gamma}{N_p \pi \sigma_i(\tau)^2}$ represents the temporal correlation function, which depends on the contrast of the emitters (γ), the average number of emitters (N_p), and σ_i. In this model, the initial segmentation is based on a preliminary estimate of (ζ_0, ψ_0), such as the peak of the pCF, which is iteratively refined using values obtained from successive fittings. Analysis is validated by the convergence of these fitting parameters.

Diffusometry and velocimetry using dual-timescale model function

After extracting the distortion-free component from the correlated data, the analysis procedure outlined in Fig. 1 is used to measure particle diffusivity changes due to glycerol concentration gradients. According to the Stokes-Einstein equation, the diffusion coefficient of particles is inversely proportional to the medium's viscosity. Therefore, areas with lower viscosity are associated with higher diffusivity, while regions with higher viscosity show reduced diffusivity. This establishes a direct relationship between local viscosity changes and particle diffusivity in the microchannel.

Experimentally, we introduced a series of glycerol concentration gradients along the length of the observation microchannel (see Fig. 5). These gradients are represented by their concentration ratio, $C_H : C_L$ (w/w%), where C_H denotes the glycerol concentration at the high-end (left side) of the microchannel, and C_L is the concentration at the low-end (right side). In Fig. 5, we calculate the local diffusion coefficient, $D(x, y)$, using the dual-timescale model function with a signal separation delay time of $\tau_s = 200$ ms for suspended nanospheres of a nominal diameter of 0.02 μm. Our approach showcases the theoretically expected decrease in diffusivity within areas of higher viscosity (corresponding to the regions of high glycerol concentration) on the left side of the microchannel (see Fig. 5 *a*). Moreover, the diffusivity values averaged over the channel width (y axis), denoted by $\overline{D}(x)$, reveal a linear diffusivity gradient counter to the direction of the applied concentration gradient in agreement with the analytical model (see supporting material). This empirical evidence proves the ability of the dual-timescale model in conducting diffusometry analyses on systems exhibiting spatiotemporal variations in the distribution of emitters.

Having confirmed the effectiveness of our dual-timescale model function for analyzing inhomogeneous systems, especially those with an ST-PDF distribution, we examine its compatibility with simpler systems that feature a stationary PDF for emitter distribution. We use the identical experimental setup is without introducing any concentration gradient. Instead, Milli-Q water is supplied continuously to the left and right inlet channels at different flow rates,

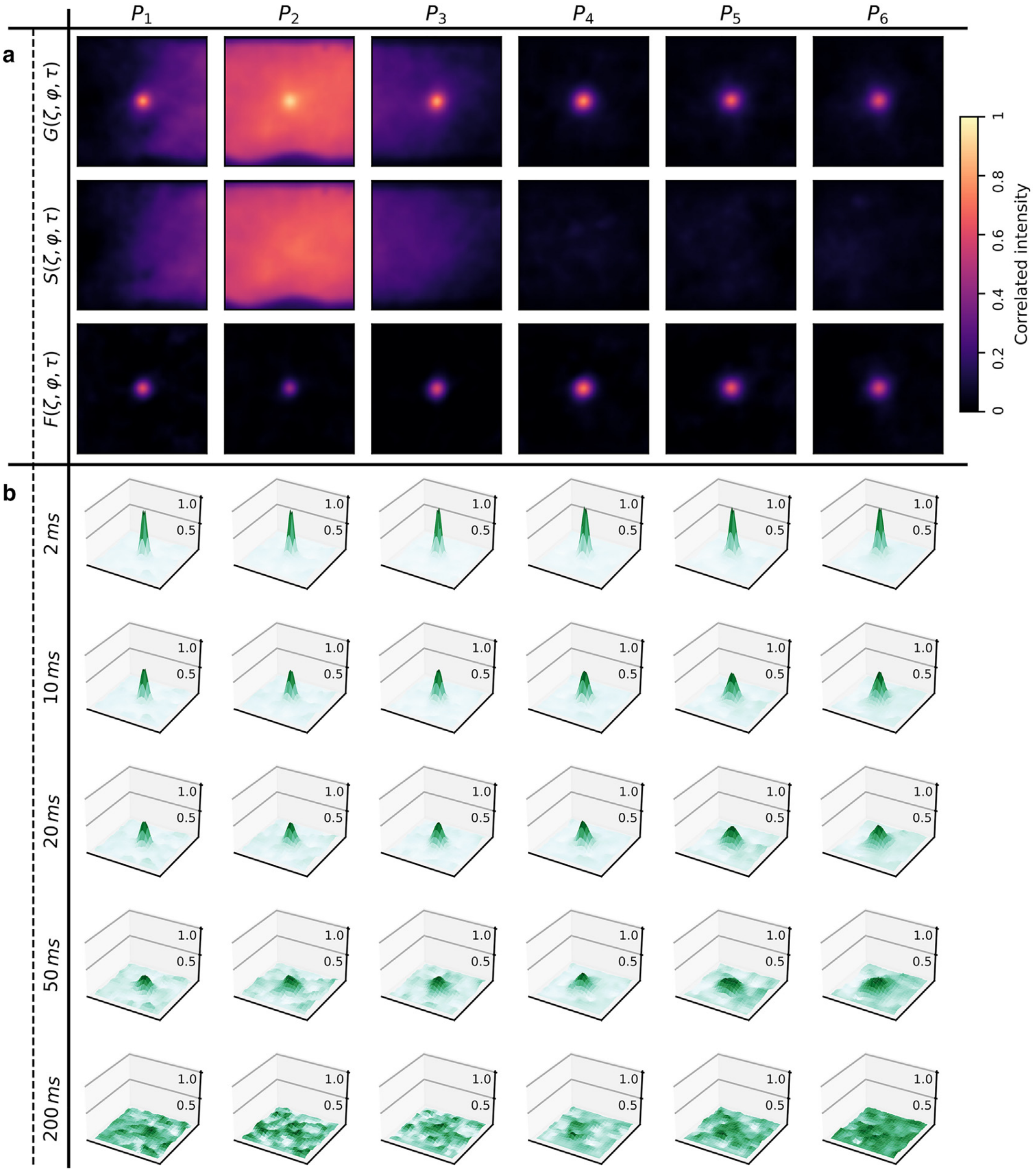

FIGURE 4 Decomposition of pCF components using the dual-timescale model function. $G(\zeta, \psi, \tau)$ values are calculated for six pixel points P_1 to P_6 marked by cyan squares in Fig. 2. (*a*) Effective separation of fast $F(\zeta, \psi)$ and slow $S(\zeta, \psi)$ components of $G(\zeta, \psi)$ at $\tau = 2$ ms, employing the dual-timescale model function delineated in Eq. 5, with a signal separation timescale $\tau_s = 200$ ms. Distortions attributed to local accumulation of nanospheres are selectively identified by the slow component. (*b*) Temporal variation of the extracted distortion-free $F(\zeta, \psi, \tau)$ within short delay times of $\tau \le \tau_s$, preserving the data set associated with diffusion and transport of nanospheres, which can be accurately modeled by Gaussian model functions. For each pixel point, values presented in (*a*) and (*b*) are normalized relative to their corresponding maximum of $G(\zeta, \psi, \tau)$ and $F(\zeta, \psi, \tau)$ at $\tau = 2$ ms, respectively. The formation of the nanosphere accumulation zone is attributed to the constant aqueous glycerol gradients of 50 and 10% (w/w%) applied at the left and right ends of the mixing microchannel, respectively.

Q_L and Q_R, respectively. Different flow rates $Q_L \neq Q_R$ create a pressure difference between the ends of the microchannel. Thus, Poiseuille flow is generated in the observation channel. (The pressure difference is reduced to a degree by the bypass channel shown in Fig. 1. Therefore, low flow rates are generated.)

Experimental evidence supporting this phenomenon is showcased in Fig. 6, which displays the velocity vectors of nanospheres with a nominal diameter of 0.02 μm under various flow rate ratios, $Q_L : Q_R$ (μL/h). These velocity vectors, represented as $V(x, y)$, were determined using our dual-timescale model function with a signal separation delay time of $\tau_s = 200$ ms. For low inlet flow rate ratios up to 200 : 5 (μL/h) no significant flow is observed. This indicates that, within this range, convective flow resulting from the imbalanced flow rates primarily diverts through

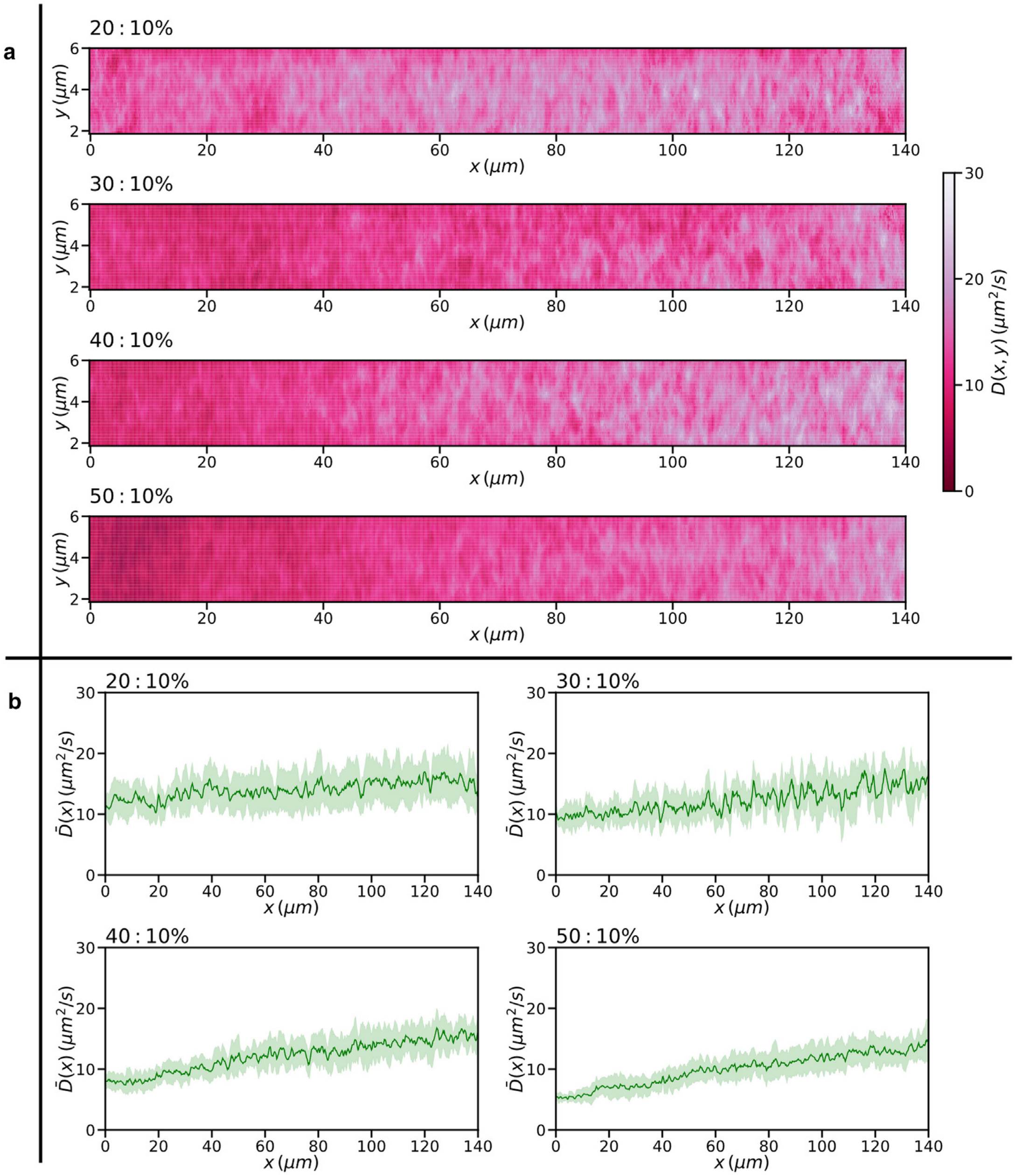

FIGURE 5 Spatial variation in particle diffusivity within an inhomogeneous medium under viscosity gradients. (*a*) The diffusivity values, $D(x,y)$, for nanospheres of 0.02 μm diameter are calculated using the dual-timescale model function using a signal separation delay time of $\tau_s = 200$ ms. The viscosity gradients are induced by glycerol concentration gradients within the observation microchannel, represented by the concentration ratios $C_H : C_L$ (w/w%). Here, C_H and C_L denote the glycerol concentrations at the microchannel's high-end (*left side*) and low-end (*right side*), respectively. (*b*), The diffusivity values averaged across the channel width (y axis), $\overline{D}(x)$, with fluctuation bandwidths indicating the standard deviation along the y axis.

the downstream parallel bypass channel. However, at substantially higher inlet flow rate ratios, such as 1000 : 5 and 2500 : 5 (μL/h) the normalized arrows and colormaps clearly indicate a convective flow direction toward the right inlet channel. Moreover, the uniformity of the velocity profiles, $u(y)$, across three distinct cross sections of each velocity field (as detailed in Fig. 6), aligns with the principle of flow continuity for incompressible fluids. Furthermore, the observed patterns of $u(y)$ values closely match with an analytical solution for the Poiseuille velocity profile in rectangular microchannels (see supporting material). These findings underscore the suitability of the introduced dual-timescale model function for systems where the correlated signals remain undistorted and can be accurately described by the standard Gaussian model function.

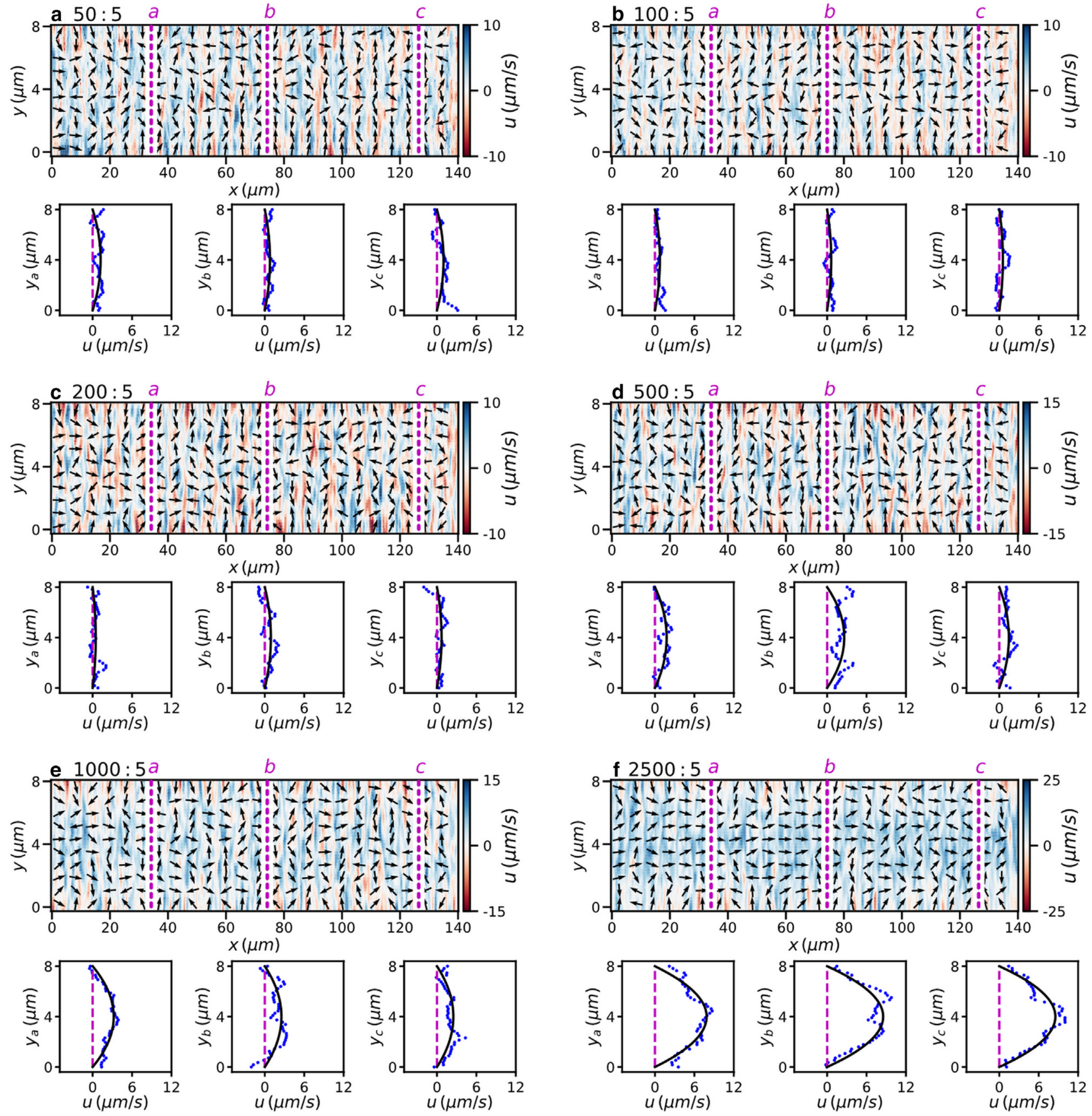

FIGURE 6 Poiseuille flow within the observation microchannel due to increasingly (*a–f*) imbalanced flow rate ratios. Velocity vectors are determined using the dual-timescale model function with a signal separation delay of $\tau_s = 200$ ms. Milli-Q water is supplied continuously at distinct flow rates Q_L and Q_R to the left and right inlet channels, respectively, with fluorescent nanospheres introduced into both feed solutions at a concentration of 2 μg/mL. The velocity fields are depicted in a colormap to illustrate the horizontal velocity component, $u_{(x,y)}$, with normalized arrows indicating the flow direction. Velocity profiles for cross sections A, B, and C are represented by fitting to the analytical model for Poiseuille flow in rectangular microchannels (*solid black lines*), as detailed in supporting material, section 3, compared against the empirically quantified values (*blue markers*).

CONCLUSION

We developed a new data processing approach for imaging-based FCS in environments where suspended fluorescent emitters are characterized with an ST-PDF distribution. Our approach overcomes the low accuracy of commonly used state-of-the-art model functions which often fall short of accurately determining diffusion and particle transport due to distorted correlated intensity data.

By extending the conventional pCF technique with a dual-timescale model function, we selectively segregate correlated data associated with rapid processes of diffusion and transport, from those distorted by changes in emitter quantity over longer timescale. This methodology is similar to time-resolved FCS (26,54,55), which distinguishes fluorescence correlations of multiple emitters based on their fluorescence lifetimes. Our technique sidesteps the need to pinpoint the exact sources of distortion, facilitating the extraction of a distortion-free data set that fully represents transport and diffusion phenomena. Thus, an extracted data set can be accurately described using standard models without requiring additional fitting parameters. Nonetheless, the presented technique falls short in cases where the fast and slow regimes overlap. This requires the dissipation of signals from transport and diffusion phenomena before the signal from the emitters' quantity and distribution starts to change. To ensure this, further quantitative analysis can be beneficial, following the visual assessment detailed in Fig. 3 *c*. See supporting material for a quantitative analysis of the corresponding time delays providing an estimate for the signal separation time delay (τ_s).

We demonstrated the ability of the dual-timescale model pCF analysis by separating drift, diffusion, and accumulation of fluorescent nanoparticles in a microfluidic proof-of-principle experiment. We believe that the method can find applications for experimental conditions associated with a temporal change in the spatial distribution of emitters, such as sedimentation (36), biomolecular binding (28), and local particle aggregation (37).

DATA AND CODE AVAILABILITY

The data sets and analysis code supporting the findings of this study are available in the Zenodo repository, accessible via Zenodo: https://doi.org/10.5281/zenodo.10961989. Additional data can be made available upon request to the corresponding author.

SUPPORTING MATERIAL

Supporting material can be found online at https://doi.org/10.1016/j.bpj.2024.08.002.

AUTHOR CONTRIBUTIONS

V.K. conducted all data acquisition and analysis, with assistance from V.J.P.B. The data processing codes were developed by V.J.P.B. and V.K. V.K. and K.M. designed the experiments and interpreted the results. V.K. drafted the manuscript with feedback from all coauthors. K.M., R.C.C., and J.H. supervised the project.

ACKNOWLEDGMENTS

We thank P.P.M.F.A. Mulder for the technical support in fabrication of the microfluidic devices and A. Jabermoradi and S. Yang for their support with the fluorescence microscopy. We thank C. Gohlke for providing a simulated data set.

DECLARATION OF INTERESTS

The authors declare no competing interests.

REFERENCES

1. Weidemann, T., J. Mücksch, and P. Schwille. 2014. Fluorescence fluctuation microscopy: A diversified arsenal of methods to investigate molecular dynamics inside cells. *Curr. Opin. Struct. Biol.* 28:69–76.
2. Elson, E. L. 2011. Fluorescence correlation spectroscopy: Past, present, future. *Biophys. J.* 101:2855–2870.
3. Ries, J., and P. Schwille. 2012. Fluorescence correlation spectroscopy. *Bioessays.* 34:361–368.
4. Yu, L., Y. Lei, …, P. Gao. 2021. A Comprehensive Review of Fluorescence Correlation Spectroscopy. *Front. Physiol.* 9:1–21.
5. Wohland, T., X. Shi, …, E. H. K. Stelzer. 2010. Single Plane Illumination Fluorescence Correlation Spectroscopy (SPIM-FCS) probes inhomogeneous three-dimensional environments. *Opt Express.* 18:10627–10641.
6. Krieger, J. W., A. P. Singh, …, J. Langowski. 2014. Dual-color fluorescence cross-correlation spectroscopy on a single plane illumination microscope (SPIM-FCCS). *Opt Express.* 22:2358–2375.
7. Berland, K. M., P. T. So, and E. Gratton. 1995. Two-photon fluorescence correlation spectroscopy: method and application to the intracellular environment. *Biophys. J.* 68:694–701.
8. Wennmalm, S., P. Thyberg, …, J. Widengren. 2009. Inverse-fluorescence correlation spectroscopy. *Anal. Chem.* 81:9209–9215.
9. Kastrup, L., H. Blom, …, S. W. Hell. 2005. Fluorescence fluctuation spectroscopy in subdiffraction focal volumes. *Phys. Rev. Lett.* 94:178104.
10. Bacia, K., and P. Schwille. 2007. Practical guidelines for dual-color fluorescence cross-correlation spectroscopy. *Nat. Protoc.* 2:2842–2856.
11. Dertinger, T., A. Loman, …, J. Enderlein. 2008. The optics and performance of dual-focus fluorescence correlation spectroscopy. *Opt Express.* 16:14353–14368.
12. Petrášek, Z., J. Ries, and P. Schwille. 2010. Scanning FCS for the Characterization of Protein Dynamics in Live Cells. *Methods Enzymol.* 472:317–343.
13. Hebert, B., S. Costantino, and P. W. Wiseman. 2005. Spatiotemporal Image Correlation Spectroscopy (STICS) Theory, Verification, and Application to Protein Velocity Mapping in Living CHO Cells. *Biophys. J.* 88:3601–3614.
14. Digman, M. A., and E. Gratton. 2009. Imaging barriers to diffusion by pair correlation functions. *Biophys. J.* 97:665–673.
15. Digman, M. A., and E. Gratton. 2011. Lessons in fluctuation correlation spectroscopy. *Annu. Rev. Phys. Chem.* 62:645–668.
16. Ries, J., M. Bayer, …, P. Schwille. 2010. Automated suppression of sample-related artifacts in Fluorescence Correlation Spectroscopy. *Opt Express.* 18:11073–11082.
17. Chojnacki, J., D. Waithe, …, C. Eggeling. 2017. Envelope glycoprotein mobility on HIV-1 particles depends on the virus maturation state. *Nat. Commun.* 8:545.
18. Hennen, J., K. H. Hur, …, J. D. Mueller. 2017. Quantitative Brightness Analysis of Protein Oligomerization in the Nuclear Envelope. *Biophys. J.* 113:138–147.
19. Hur, K. H., and J. D. Mueller. 2015. Quantitative brightness analysis of fluorescence intensity fluctuations in E. coli. *PLoS One.* 10:e0130063.
20. Kohler, J., K. H. Hur, and J. D. Mueller. 2023. Autocorrelation function of finite-length data in fluorescence correlation spectroscopy. *Biophys. J.* 122:241–253.
21. Latreille, P. L., M. Le Goas, …, X. Banquy. 2022. Scratching the Surface of the Protein Corona: Challenging Measurements and Controversies. *ACS Nano.* 16:1689–1707.

22. Ridgeway, W. K., D. P. Millar, and J. R. Williamson. 2013. Vectorized data acquisition and fast triple-correlation integrals for Fluorescence Triple Correlation Spectroscopy. *Comput. Phys. Commun.* 184:1322–1332.

23. Ries, J., and P. Schwille. 2008. New concepts for fluorescence correlation spectroscopy on membranes. *Phys. Chem. Chem. Phys.* 10:3487–3497.

24. Wang, H., Y. Lin, …, G. U. Nienhaus. 2018. The protein corona on nanoparticles as viewed from a nanoparticle-sizing perspective. *Wiley Interdiscip. Rev. Nanomed. Nanobiotechnol.* 10:e1500–e1509.

25. Guo, S. M., J. He, …, M. Bathe. 2012. Bayesian approach to the analysis of fluorescence correlation spectroscopy data II: Application to simulated and in vitro data. *Anal. Chem.* 84:3880–3888.

26. Kapusta, P., R. Macháň, …, M. Hof. 2012. Fluorescence lifetime correlation spectroscopy (FLCS): Concepts, applications and outlook. *Int. J. Mol. Sci.* 13:12890–12910.

27. Kolin, D. L., S. Costantino, and P. W. Wiseman. 2006. Sampling Effects, Noise, and Photobleaching in Temporal Image Correlation Spectroscopy. *Biophys. J.* 90:628–639.

28. Liu, C., Y. L. Liu, …, H. C. Yeh. 2016. Single-Molecule Tracking and Its Application in Biomolecular Binding Detection. *IEEE J. Sel. Top. Quant. Electron.* 22:6804013–6804076.

29. Wohland, T., R. Rigler, and H. Vogel. 2001. The standard deviation in fluorescence correlation spectroscopy. *Biophys. J.* 80:2987–2999.

30. Seltmann, A., P. Carravilla, …, D. Waithe. 2024. Neural network informed photon filtering reduces fluorescence correlation spectroscopy artifacts. *Biophys. J.* 123:745–755.

31. Kim, S. A., K. G. Heinze, and P. Schwille. 2007. Fluorescence correlation spectroscopy in living cells. *Nat. Methods.* 4:963–973.

32. Di Rienzo, C., F. Cardarelli, …, E. Gratton. 2016. Diffusion Tensor Analysis by Two-Dimensional Pair Correlation of Fluorescence Fluctuations in Cells. *Biophys. J.* 111:841–851.

33. Di Rienzo, C., E. Gratton, …, F. Cardarelli. 2013. Fast spatiotemporal correlation spectroscopy to determine protein lateral diffusion laws in live cell membranes. *Proc. Natl. Acad. Sci. USA.* 110:12307–12312.

34. Gaus, K. 2016. Biologists Wanted: New Fluorescence Fluctuation Tools for Cell Biology. *Biophys. J.* 111:677–678.

35. Khandan, V., V. Boerkamp, …, K. Mathwig. 2022. Viscophoretic particle transport. Preprint at arXiv. https://doi.org/10.48550/arXiv.2212.11503.

36. Xu, F. 2018. Review of analytical studies on TiO2 nanoparticles and particle aggregation, coagulation, flocculation, sedimentation, stabilization. *Chemosphere.* 212:662–677.

37. He, J., C. Li, …, Y. Wang. 2019. Tumor Targeting Strategies of Smart Fluorescent Nanoparticles and Their Applications in Cancer Diagnosis and Treatment. *Adv. Mater.* 31:e1902409–e1902431.

38. Jerabek-Willemsen, M., T. André, …, D. Breitsprecher. 2014. MicroScale Thermophoresis: Interaction analysis and beyond. *J. Mol. Struct.* 1077:101–113.

39. Shim, S. 2022. Diffusiophoresis, Diffusioosmosis, and Microfluidics: Surface-Flow-Driven Phenomena in the Presence of Flow. *Chem. Rev.* 122:6986–7009.

40. Lightley, J., S. Kumar, …, P. M. W. French. 2023. openFrame: A modular, sustainable, open microscopy platform with single-shot, dual-axis optical autofocus module providing high precision and long range of operation. *J. Microsc.* 292:64–77. https://doi.org/10.1111/jmi.13219.

41. Yang, S., M. Takeuchi, …, J. Hohlbein. 2024. Adapting cryogenic correlative light and electron microscopy (cryo-CLEM) for food oxidation studies. *Food Struct.* 40:100365.

42. Jabermoradi, A., S. Yang, …, J. Hohlbein. 2022. Enabling single-molecule localization microscopy in turbid food emulsions. *Philos. Trans. A Math. Phys. Eng. Sci.* 380:20200164.

43. Edelstein, A. D., M. A. Tsuchida, …, N. Stuurman. 2014. Advanced methods of microscope control using μManager software. *J. Biol. Methods.* 1:e10.

44. Edelstein, A., N. Amodaj, …, N. Stuurman. 2010. Computer Control of Microscopes Using μManager. *Curr. Protoc. Mol. Biol.* Chapter 14:Unit14.20-14.20.17.

45. Martens, K. J. A., S. P. B. Van Beljouw, …, J. Hohlbein. 2019. Visualisation of dCas9 target search in vivo using an open-microscopy framework. *Nat. Commun.* 10:3552. https://doi.org/10.1038/s41467-019-11514-0.

46. Ferreira, A. G., A. P. Egas, …, L. Q. Lobo. 2017. The viscosity of glycerol. *J. Chem. Thermodyn.* 113:162–182.

47. Marbach, S., H. Yoshida, and L. Bocquet. 2020. Local and global force balance for diffusiophoretic transport. *J. Fluid Mech.* 892:A6.

48. de Haan, H. W., M. V. Chubynsky, and G. W. Slater. 2012. Monte Carlo Approaches for Simulating a Particle at a Diffusivity Interface and the "Ito–Stratonovich Dilemma.". Preprint at arXiv. https://doi.org/10.48550/arXiv.1208.5081.

49. Yang, M., and M. Ripoll. 2013. Brownian motion in inhomogeneous suspensions. *Phys. Rev. E Stat. Nonlinear Soft Matter Phys.* 87:062110.

50. Wiener, B., and D. Stein. 2018. Electrokinetic Current Driven by a Viscosity Gradient. Preprint at arXiv. https://doi.org/10.48550/arXiv.1807.09106.

51. Vinze, P. M., A. Choudhary, and S. Pushpavanam. 2021. Motion of an active particle in a linear concentration gradient. *Phys. Fluids.* 33:1–13.

52. Velegol, D., A. Garg, …, M. Kumar. 2016. Origins of concentration gradients for diffusiophoresis. *Soft Matter.* 12:4686–4703.

53. Hebert, B., S. Costantino, and P. W. Wiseman. 2005. Spatiotemporal image correlation spectroscopy (STICS) theory, verification, and application to protein velocity mapping in living CHO cells. *Biophys. J.* 88:3601–3614.

54. Böhmer, M., M. Wahl, …, J. Enderlein. 2002. Time-resolved fluorescence correlation spectroscopy. *Chem. Phys. Lett.* 353:439–445.

55. Ghosh, A., N. Karedla, …, J. Enderlein. 2018. Fluorescence lifetime correlation spectroscopy: Basics and applications. *Methods.* 140–141:32–39.

Biophysical Journal, Volume *124*

Supplemental information

Addressing spatiotemporal signal variations in pair correlation function analysis

Vahid Khandan, Vincent J.P. Boerkamp, Ryan C. Chiechi, Johannes Hohlbein, and Klaus Mathwig

1. Mechanisms of particle accumulation

The glycerol concentration gradient established within the mixing microchannel creates an inhomogeneous medium characterized by spatial variations in the viscosity of the aqueous solution. Consequently, suspended nanospheres within this medium exhibit different diffusivities, potentially resulting in viscophoretic drift, as depicted in Figure S1. Furthermore, the concentration gradient itself can independently trigger diffusiophoretic drift and diffusioosmotic flow. Additionally, disparities in geometry, fluid properties, and flow rates between the side channels may generate a pressure difference across the microchannel, leading to Poiseuille flow velocity, also shown in Figure S1. These mechanisms, whether operating independently or synergistically, exert a significant influence on the movement of fluorescent nanospheres in different directions. I.e., non-equilibrium conditions are established that convert an initially uniform distribution of fluorescent nanospheres into localized accumulations, as illustrated in Figure S2.

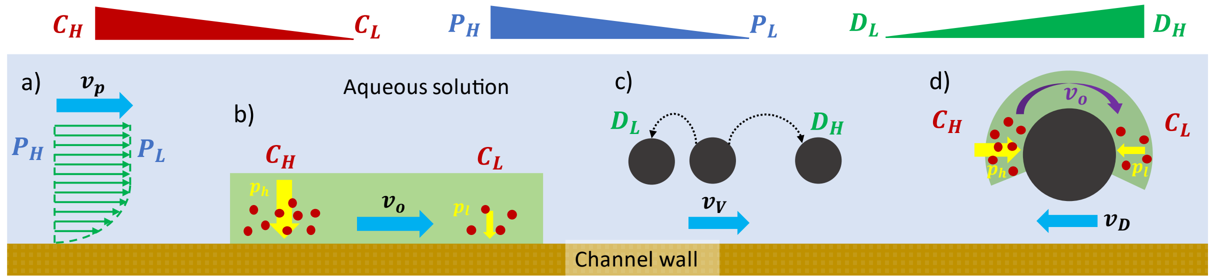

Figure S1. *Schematics of transport mechanisms influenced by applied glycerol concentration gradient. (a) Poiseuille flow velocity* (v_P) *arises due to the pressure difference* $(P_H\!:\!P_l)$ *between the side channels, attributed to disparities in geometry, fluid properties, and flow rates, affecting the flow dynamics within the side channels. (b) Diffusioosmosis flow* (v_O) *occurs within a thin layer adjacent to the channel walls, driven by the pressure difference* $(p_h\!:\!p_l)$ *that develops close to the walls due to the applied concentration gradient* $(C_H\!:\!C_L)$*. (c) Viscophoretic drift* (v_V) *emerges from the diffusivity gradient* $(D_H\!:\!D_L)$ *created by the concentration gradient* $(C_H\!:\!C_L)$*. (d) Diffusiophoretic drift* (v_D) *is a consequence of the diffusioosmotic flow within a thin layer surrounding the particle, triggered by the concentration gradient* $(C_H\!:\!C_L)$*. The directions of potential velocities* v_P*,* v_O *and* v_V *extend from the high concentration side to the lower concentration end of the mixing microchannel, whereas* v_D *moves in the reverse direction.*

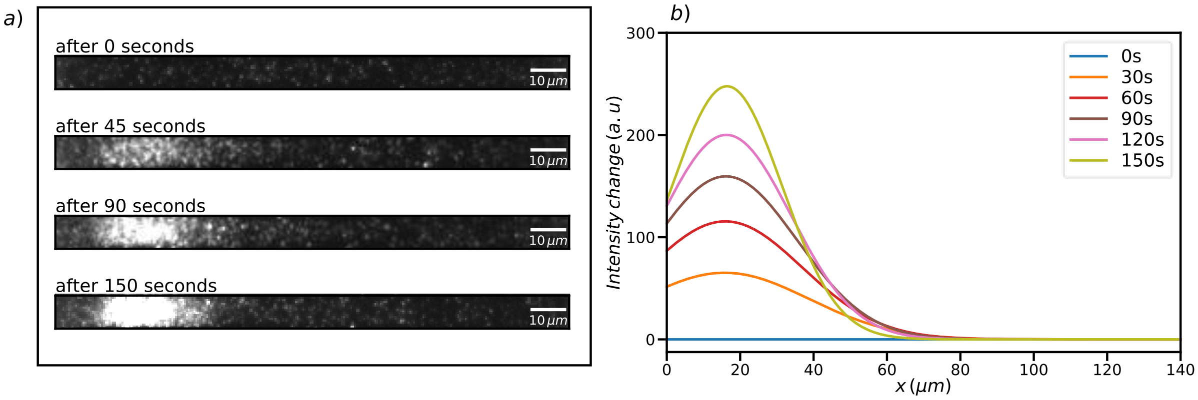

Figure S2. *Nanosphere accumulation in response to an established glycerol concentration gradient. The gradient is characterized by the ratio* $C_H\!:\!C_L(w\!:\!w\%)$*, where* C_H *and* C_L *denote the stable glycerol concentrations at the high-viscosity (left) and low-viscosity (right) ends of the microchannel, respectively. (a) Snapshot images from within the gradient region illustrate a local increase in nanosphere concentration. (b) This increase is accompanied by a corresponding rise in pixel intensities, adhering to a scaled normal distribution pattern that intensifies over time. This pattern is fitted to the averaged intensity changes across the width of the microchannel.*

2. Diffusivity gradient induced by viscosity gradient

The viscosity of a mixture comprised of two miscible solutions can be directly determined from the viscosity of the base solutions, η_A and η_B, as well as their respective volume fractions, ϕ_A and ϕ_B, such that $\eta_{mix} = \eta_A^{\phi_A} . \eta_B^{\phi_B}$, where $\phi_A + \phi_B = 1$. As a result, the viscosity gradient induced within a mixing microchannel exhibiting stable boundary condition, as illustrated in Figure S3, can be described as:

$$\eta(x) = \eta_H^{\phi(x)} . \eta_L^{(1-\phi(x))} \qquad \text{Equation S1}$$

Here, η_H and η_L represent the dynamic viscosities of the solutions with high and low glycerol concentrations, respectively, while $\phi(x)$ denotes the volume fraction of the high glycerol concentration solution.

Under steady-state conditions and in the absence of convective flow within the gradient region, it can be assumed that the diffusion of glycerol molecules follows a Fickian distribution, and $\phi(x)$ complies with

$$\frac{\partial}{\partial x}\left(D_o(x)\frac{\partial \phi}{\partial x}\right) = 0, \qquad \text{Equation S2}$$

where $D_o(x)$ represents the diffusion coefficient of glycerol molecules.

Extracting $\phi(x)$ from Equation S1, we obtain

$$\phi(x) = \frac{Ln(\frac{\eta(x)}{\eta_L})}{Ln(\frac{\eta_H}{\eta_L})} . \qquad \text{Equation S3}$$

Then,

$$\frac{\partial \phi}{\partial x} = \frac{1}{\eta(x)\, Ln(\frac{\eta_H}{\eta_L})} . \frac{\partial \eta(x)}{\partial x} . \qquad \text{Equation S4}$$

The diffusion coefficient can also be estimated with the Stokes-Einstein equation as

$$D_o(x) = \frac{k_B T}{6\pi r\, \eta(x)} . \qquad \text{Equation S5}$$

Here, k_B is the Boltzmann constant, T is the absolute temperature, and r represents the radius of glycerol molecules. By substituting Equation S4 and Equation S5 in Equation S2, and integrating over Equation S2, we obtain

$$\frac{\partial \eta(x)}{\partial x} = \eta(x)^2 \frac{C_1}{A}, \qquad \text{Equation S6}$$

where $A = \frac{k_B T}{6\pi r\, Ln(\frac{\eta_H}{\eta_L})}$, and C_1 is the constant that appears during integration. Equation S6 has the solution

$$\eta(x) = \frac{1}{C_2 - \left(\frac{C_1}{A}\right)x} . \qquad \text{Equation S7}$$

By applying boundary conditions illustrated in Figure S, the viscosity gradient can be expressed as

$$\eta(x) = \left(\frac{1}{\eta_H} - \frac{x}{L}\left(\frac{1}{\eta_H} - \frac{1}{\eta_L}\right)\right)^{-1} . \qquad \text{Equation S8}$$

By determining the viscosity gradient, the diffusivity gradient of a Brownian particle with a diameter of d can be estimated using the Stokes-Einstein equation as

$$D(x) = \frac{k_B T}{3\pi d} . \left(\frac{1}{\eta_H} - \frac{x}{L}\left(\frac{1}{\eta_H} - \frac{1}{\eta_L}\right)\right). \qquad \text{Equation S9}$$

By defining $D_H = \frac{k_B T}{3\pi d \eta_H}$ and $D_L = \frac{k_B T}{3\pi d \eta_L}$ as the diffusion coefficient corresponding to the high and low concentration side ($D_H < D_L$ as $\eta_H > \eta_L$), respectively, the diffusivity gradient can be reformulated as

$$D(x) = D_H - \frac{x}{L}(D_H - D_L). \qquad \text{Equation S10}$$

In conclusion, in the presented mixing channel under steady-state conditions, the absence of convective flow results in a linear glycerol concentration gradient, which induces heterogeneity with a linear diffusivity gradient. Conversely, a linear distribution of diffusivity gradient also implies the absence of convective flow in the presented system.

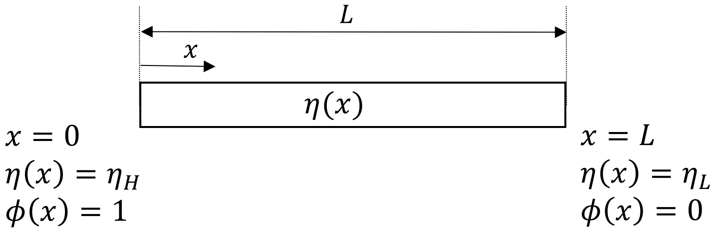

Figure S3. *Schematic representation of the viscosity gradient induced within a microchannel under steady-state boundary conditions.*

3. Poiseuille flow in microchannels with a rectangular cross section

The analytical solution for Poiseuille flow velocity in a rectangular duct is given by (1)

$$u(y,z) = \frac{-\frac{dp}{dx}}{\mu}\left(\frac{y(w-y)}{2} - \frac{4w^2}{\pi^3}\sum_{n=1}^{\infty}\frac{I_n}{(2n-1)^3}\right), \qquad \text{Equation S11}$$

$$\text{with} \quad I_n = \frac{\sinh(B_n z)\,\sinh\,(B_n(h-z))}{\sinh\,(B_n h)}\sin(B_n y) \;\; \text{and}\; B_n = \frac{(2n-1)\pi}{w}.$$

In this expression, w and h represent the width and height of the observation microchannel, as illustrated in Figure S4 , $\frac{dp}{dx}$ denotes the generated pressure difference, and μ refers to the dynamic viscosity of the fluid.

The effect of alterations in the aspect ratio ($\frac{w}{h}$) of microchannels on the shape of the velocity profile is illustrated in Figure S4B-D. As demonstrated, for high aspect ratios (e.g., nanochannels), the velocity values exhibit a distribution with a flat peak. While, for aspect ratios approaching unity, the distribution closely resembles a parabolic shape. These changes in the velocity profile shape are also evident in the values of the averaged Poiseuille flow velocity across the channel thickness, $u(y) = \frac{1}{h}\int_0^h u(y,z)dz$, as shown in Figure S4E.

Considering that the velocity field determined using pair correlation function (pCF) analysis is a two-dimensional map, it is crucial to consider the averaged Poiseuille flow velocity across the channel thickness, $u(y)$, for fitting the experimental data. Moreover, since the microchannel's width and height are known to be $h = 2$ µm and $w = 8$ µm, and the fluid's viscosity is also determined ($\mu = 1.005\ cp$), the applied pressure difference term, $\mathrm{d}p/\mathrm{d}x$, remains the only fitting parameter to determine the induced velocity profile presented in Figure 6 in the main text.

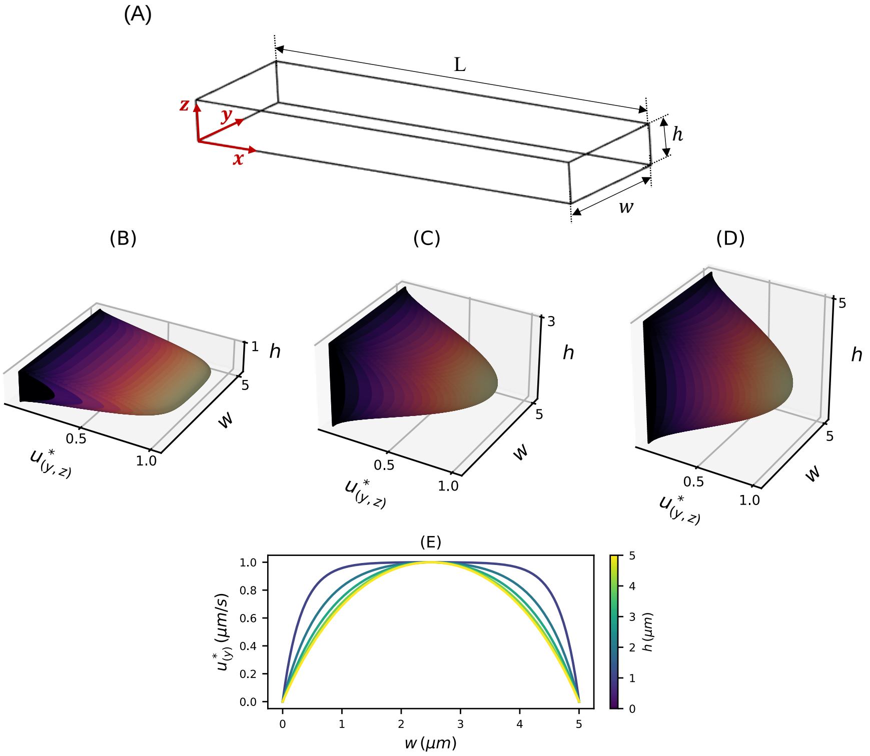

Figure S4. *Poiseuille Flow Velocity in Rectangular Microchannels. (A) Schematic representation of a rectangular microchannel with designated dimensions. Analytical solution illustrations for varying channel thicknesses (h) while maintaining constant channel width (w): (B-D) Three-dimensional view,* $u(y,z)$*, and (E) Two-dimensional perspective,* $u(y)$ *averaged across channel thicknesses (z-axis). The values are normalized relative to the corresponding maximum velocity, with pressure difference and viscosity considered unity.*

4. Determining the transient phase (Λ_2) using Normalized Root Mean Squared Deviation (NRMSD) analysis of the pCF

The transient phase starts with the complete dissipation of the fast component, $F(\zeta,\psi,\tau)$, over short delay times at τ_{FT} and ends with the onset of variations in the slow component, $S(\zeta,\psi,\tau)$, at extended delay times at τ_{ST}. Determining the transient phase is crucial as it defines the interval for valid estimation of the signal separation delay time, τ_s, necessary to distinguish between $S(\zeta,\psi,\tau)$ and $F(\zeta,\psi,\tau)$ signals. We quantitatively determine the values of τ_{FT} and τ_{ST} directly from NRMSD values of pCF, $\delta G(\Delta)$, as expressed in Equation 6.

The dissipation of the $F(\zeta,\psi,\tau)$ signal within the initial phase, Λ_1, is defined by a rapid increase in $\delta G(\Delta)$ values, which is followed by reaching a plateau indicating the transient phase Λ_2. These two phases can be described empirically based on the experimental results shown in Figure 3 as:

$$\delta G(\Delta) = c_1(1 - c_2 e^{-c_3\Delta + c_4}), \quad \text{for} \quad \Delta \leq \tau_{ST}.$$

Equation S12

Here, the parameters c_1, c_2, c_3 and c_4 are fitting parameters determined empirically from the $\delta G(\Delta)$ values. As Δ increases, the exponential term $e^{-c_3 x + c_4}$ approaches zero, making $\delta G(\Delta)$ approach c_1 at the plateau within the phase Λ_2. To quantify this, a threshold ϵ can be defined as $\delta G(\Delta) = c_1 - \epsilon$. The threshold ϵ determines when $\delta G(\Delta)$ is close enough to the plateau and $F(\zeta,\psi,\tau)$ is dissipated. Then, the estimation of τ_{FT} is:

$$\tau_{FT} = \frac{c_4 - \ln\left(\frac{\epsilon}{c_1 c_2}\right)}{c_3}.$$

Equation S13

On the other hand, the final phase, Λ_3, is accompanied with a sustained growth in $\delta G(\Delta)$ resulting from the increase in the number of fluorescent nanospheres within the accumulation region. Therefore, under steady-state conditions with no significant photobleaching, the accumulation rate remains constant, leading to a linear increase in $\delta G(\Delta)$ values, described as

$$\delta G(\Delta) = c_1(c_1 - c_2) + c_5\Delta, \quad \text{for} \quad \Delta > \tau_{ST}. \qquad \text{Equation S14}$$

By combining Equation S12 and Equation S14 and fitting over the experimental $\delta G(\Delta)$ values, τ_{ST} can be directly determined as an additional fitting parameter, denoted as of $c_6 = \tau_{ST}$. Then, the final model function will be expressed as:

$$\delta G(\Delta) = c_1\left(1 - c_2 e^{-c_3\Delta + c_4}\right), \quad \text{for} \quad \Delta \leq c_6 + \qquad \text{Equation S15}$$

$$c_1(c_1 - c_2) + c_5\Delta, \quad \text{for} \quad \Delta > c_6.$$

We employed this approach to quantify τ_{ST} and τ_{FT} for $\delta G(\Delta)$ values as shown in Figure 3 of the main text. As shown in Figure S5, the determined transient phase is in a good agreement within the range 200 ms $\leq \tau_s \leq$ 300 ms, (see Figure 3c). In addition, the transient phase for point P_2, which is situated in the middle of the accumulation region, is shorter than that of the other two points, P_1 and P_3, located at the corners of the accumulation region. This aligns with the observation that the final phase for points with a stronger S component starts earlier than for those with a weaker S component.

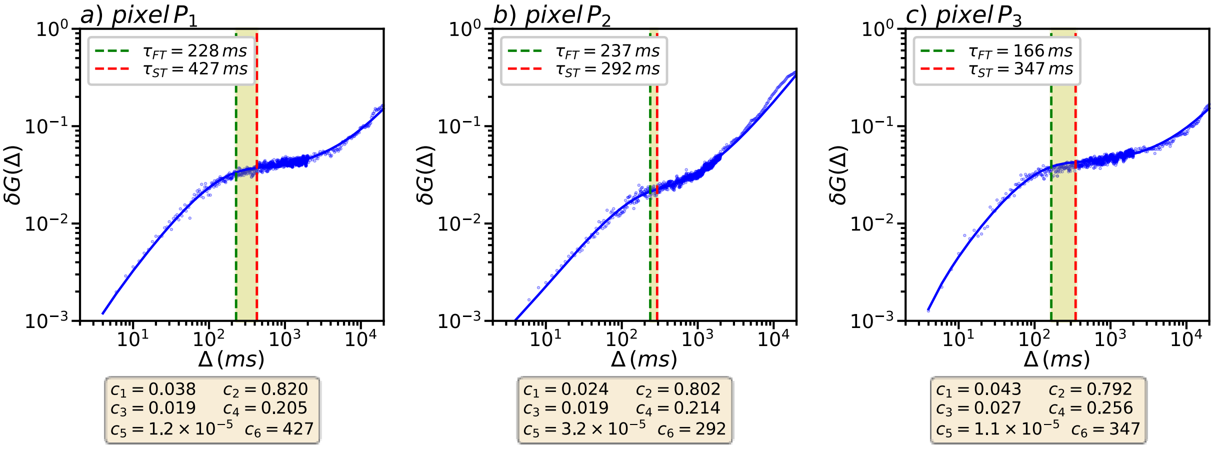

Figure S5. *Quantifying the time delays τ_{ST} and τ_{FT} for three specific pixels a) P_1, b) P_2, c) P_3 as highlighted in Figure 2. The scatter plot with blue dots represents the experimental values of $\delta G(\Delta)$, previously shown in Figure 3. The solid blue lines depict the empirical model functions based on Equations S12 and S14. The estimated values of τ_{ST} and τ_{FT} are marked with red and green dashed lines, respectively, for the threshold $\epsilon = 0.1c_1$. The gray region indicates the transient phase, which is critical for the valid estimation of τ_s.The details of the corresponding fitting parameters are provided in the box beneath each graph.*

Reference

1. Boussinesq, J. 1868. Mémoire sur l'influence des Frottements dans les Mouvements Réguliers des Fluids. *Math. Pures Appl.* 13:377–424.